



RESEARCH ARTICLE

10.1029/2018JA025354

Ion Injection Triggered EMIC Waves in the Earth's Magnetosphere

Key Points:

- Substorm ion injections can trigger EMIC waves; a decrease in the magnetic field magnitude is associated with the arrival of injected ions
- Injection signatures are observed at GOES, Van Allen Probe A, and LANL spacecraft; energy and pitch angle dispersion are observed by Van Allen Probe
- Drift paths of injected ions/electrons from various LANL spacecraft are traced back to find their injection location at 20:00 MLT

B. Remya^{1,2,3}, D. G. Sibeck², A. J. Halford⁴, K. R. Murphy^{2,5}, G. D. Reeves⁶, H. J. Singer⁷, J. R. Wygant⁸, G. Farinas Perez^{2,3}, and S. A. Thaller⁸

¹Indian Institute of Geomagnetism, Navi Mumbai, India, ²NASA Goddard Space Flight Center, Greenbelt, Maryland, USA, ³Department of Physics, Catholic University of America, Washington, DC, USA, ⁴Space Sciences Department, The Aerospace Corporation, El Segundo, CA, USA, ⁵Department of Astronomy, University of Maryland, College Park, MD, USA, ⁶Los Alamos National Laboratory, Los Alamos, NM, USA, ⁷NOAA Space Weather Prediction Center, Boulder, CO, USA, ⁸School of Physics and Astronomy, University of Minnesota, Minneapolis, MN, USA

Correspondence to:

B. Remya, remyaphysics@gmail.com

Citation:

Remya, B., Sibeck, D. G., Halford, A. J., Murphy, K. R., Reeves, G. D., Singer, H. J., et al. (2018). Ion injection triggered EMIC waves in the Earth's magnetosphere. *Journal of Geophysical Research: Space Physics*, 123. <https://doi.org/10.1029/2018JA025354>

Received 13 FEB 2018
Accepted 29 MAY 2018
Accepted article online 4 JUN 2018

Abstract

We present Van Allen Probe observations of electromagnetic ion cyclotron (EMIC) waves triggered solely due to individual substorm-injected ions in the absence of storms or compressions of the magnetosphere during 9 August 2015. The time at which the injected ions are observed directly corresponds to the onset of EMIC waves at the location of Van Allen Probe A ($L = 5.5$ and 18:06 magnetic local time). The injection was also seen at geosynchronous orbit by the Geostationary Operational Environmental Satellite and Los Alamos National Laboratory spacecraft, and the westward(eastward) drift of ions(electrons) was monitored by Los Alamos National Laboratory spacecraft at different local times. The azimuthal location of the injection was determined by tracing the injection signatures backward in time to their origin assuming a dipolar magnetic field of Earth. The center of this injection location was determined to be close to $\sim 20:00$ magnetic local time. Geostationary Operational Environmental Satellite and ground magnetometer responses confirm substorm onset at approximately the same local time. The observed EMIC wave onsets at Van Allen Probe were also associated with a magnetic field decrease. The arrival of anisotropic ions along with the decrease in the magnetic field favors the growth of the EMIC wave instability based on linear theory analysis.

1. Introduction

Electromagnetic ion cyclotron (EMIC) waves are believed to play a major role in the Earth's radiation belt dynamics. These waves are a strong source for pitch angle scattering of ring current ions (Cornwall et al., 1970; Keika et al., 2006; Kennel & Petschek, 1966; Shoji & Omura, 2014; Tsurutani & Lakhina, 1997). EMIC waves can also resonate with relativistic electrons and scatter them into the loss cone, leading to enhanced atmospheric precipitation (Jordanova et al., 2008; Kubota et al., 2015; Meredith et al., 2003; Miyoshi et al., 2008; Remya et al., 2015; Summers et al., 1998; Thorne & Kennel, 1971; Tsurutani et al., 2016). EMIC waves are also known to heat cold plasma populations by resonating with the thermal electrons and ions (Thorne & Horne, 1992; Yuan et al., 2014; Zhang et al., 2010; Zhou et al., 2013). To better understand and quantify their role in magnetospheric heating and loss processes, it is extremely important to comprehend the conditions under which these waves are generated. The geomagnetic activity and the local magnetic and plasma conditions for which these waves are or are not triggered have to be well characterized to provide a better understanding of these phenomena and to improve inputs for global modeling of radiation belts and ring current dynamics.

EMIC waves are known to be generated by anisotropic ($T_{\perp}/T_{\parallel} > 1$) distribution of ring current ions with energies of ~ 10 to 100 keV (Cornwall, 1965; Kennel & Petschek, 1966). There are two possible ways this can happen: First, on the nightside, ions of ~ 10 - to 100-keV energies can enter the inner magnetosphere via substorm injection (Elkington et al., 2005; Thorne et al., 1974) or during ring current enhancements occurring during geomagnetic storms (Cornwall & Schulz, 1971; Vasyliunas, 1976). During their earthward motion, these ions are adiabatically heated due to betatron acceleration resulting in a $T_{\perp} > T_{\parallel}$ temperature anisotropy. Second, on the dayside, remnant ~ 10 - to 100-keV ions can be betatron accelerated via intermittent solar wind compressions of the magnetosphere by interplanetary shocks or solar wind pressure pulses, leading to EMIC wave generation (Olson & Lee, 1983; Southwood & Kivelson, 1975). The energetic proton distribution near the dayside

magnetopause are marginally stable and could easily become unstable for even a small abrupt change in solar wind ram pressure leading to the growth of EMIC waves in the dayside (Anderson & Hamilton, 1993).

Several statistical studies employing satellite observations have demonstrated the occurrence rates of EMIC waves in different L-MLT sectors and their relationship to geomagnetic activity using the AE, SYM-H, and Kp indices. Kasahara et al. (1992) studied Akebono satellite observations and showed that the occurrence rates of EMIC waves increased in the 17:00–20:00 magnetic local time (MLT) region for high Kp values ($Kp > 7$). The occurrence rate of EMIC waves in the noon and afternoon (12:00–18:00 MLT) sectors were also found to increase during increased geomagnetic activity ($AE > 300$; Halford et al., 2016; Keika et al., 2013; Meredith et al., 2014; Saikin et al., 2016; Usanova et al., 2012). EMIC waves are also observed over a wide range of L shells, ranging from $L = 3$ to $L = 10$ with higher occurrence rates at large L values, irrespective of local time (Anderson et al., 1992; Usanova et al., 2012).

The relation of EMIC wave occurrence to geomagnetic storms is considered very important and has been explored in detail. The occurrence of EMIC waves during different phases of geomagnetic storms has been investigated by many, for example, Wentworth (1964), Anderson et al. (1992), Erlandson and Ukhorskiy (2001), Li et al. (2007), Engebretson et al. (2008), Halford et al. (2010), Wang et al. (2016), Tetrick et al. (2017), and references therein. Most of the satellite-based studies suggest that the EMIC wave occurrence peaks during the onset and main phase of geomagnetic storms (Anderson et al., 1992; Bräysy et al., 1998; Halford et al., 2010, 2016). This is in good agreement with the modeling studies (Jordanova et al., 2001; Khazanov et al., 2006). The EMIC waves triggered at the onset of a storm or during sudden impulses (SIs) result from the magnetospheric compression on the dayside. During the main phase of storms, there is an increase of injected hot ring current ions that overlap with the cold plasmaspheric density lowering the EMIC instability threshold and triggering the generation of EMIC waves on the duskside (Criswell, 1969; Fraser et al., 2005; Kozyra et al., 1984). This leads to higher occurrence rates in the afternoon sector.

In contrast to satellite studies, ground-based studies have demonstrated that the EMIC wave occurrence peaks within several days after the storm has reached the minimum Dst (Bortnik et al., 2008; Engebretson et al., 2008; Heacock & Akasofu, 1973; Posch et al., 2010; Wentworth, 1964). A broadband signal on the ground may mask the EMIC wave frequencies during the main phase of the storm and hence lead to lower occurrence rates (Bortnik et al., 2008; Engebretson et al., 2008). It is also possible that the EMIC waves are attenuated in the ionosphere during the main phase of a storm.

EMIC waves are very well known to be stimulated by magnetospheric compressions on the dayside (Olson & Lee, 1983). Interplanetary shocks or other kinds of solar wind pressure pulses (e.g., SIs) impinge on the magnetosphere leading to enhanced solar wind ram pressure and thereby compressing the dayside magnetosphere. This suggests that some continuous pulsations (Pc1 waves), which are the ground-based signatures of EMIC waves, result from being stimulated by or are enhanced concurrently with the start of SIs (Kangas et al., 1986; Southwood & Kivelson, 1975; Troitskaya, 1967). This has been confirmed by many in situ satellite-based studies that report either the onset or enhancement of EMIC waves in association with the compressions in the magnetosphere (Allen et al., 2016; Anderson & Hamilton, 1993; Cho et al., 2016; Engebretson et al., 2002; Ishida et al., 1987; Kim et al., 2017; Park et al., 2016; Tsurutani et al., 2001; Usanova et al., 2012). As sudden compressions are most pronounced on the dayside, EMIC waves during sudden compressions are predominantly seen to occur in the dayside subsolar outer magnetosphere (Anderson et al., 1992; Erlandson et al., 1990; Min et al., 2012; Usanova et al., 2012).

Even though high geomagnetic activity favors EMIC wave growth, there are also nonstorm time and quiet time EMIC waves observed in the magnetosphere. Saikin et al. (2016) examined the global distribution of EMIC waves seen by the Van Allen Probes for various levels of geomagnetic activity and suggested that most events during low levels of auroral electrojet (AE) and nonstorm time EMIC events occur in the prenoon sector. The prenoon/dawnside EMIC waves have also been reported using Time History of Events and Macroscale Interactions during Substorms (Usanova et al., 2012) and Van Allen Probes (Engebretson et al., 2015) observations. The events were found to be associated with compressions of the dayside magnetosphere. Park et al. (2016) analyzed EMIC waves during quiet ($Kp < 1$) geomagnetic conditions over a 2-year period from 2007 to 2008 using geosynchronous measurements and suggested that unlike magnetically disturbed times (i.e., storm and/or substorm), quiet time EMIC waves mostly occur in the dawn (~06:00 MLT) to afternoon (~16:00 MLT) sector with a peak around 11:00–12:00 MLT (see also Kim et al., 2016). Studies suggest that solar wind dynamic pressure variations are a more important parameter than AE and SYM-H for quiet time EMIC wave occurrence

(Halford et al., 2016; Meredith et al., 2014). All these statistical studies focused on providing an overall perspective on the distribution pattern of EMIC waves at different L-MLT sectors in association with different geomagnetic indices.

The present study focuses on a space-based observation of EMIC waves triggered solely due to individual substorm-injected ions in the absence of storms or compressions of the magnetosphere. There have been many ground-based observations of continuous (Pc) and irregular (Pi) pulsations associated with the onset of substorms (Akasofu, 1968; Clilverd et al., 2015; Fukunishi, 1973; Gendrin, 1970; Heacock, 1967; Jacobs, 1970; Yahnina et al., 2003). Søråas et al. (1980) studied intervals of pulsations with diminishing periods (IPDPs) on the ground and found a simultaneous increase in 40- to 60-keV proton fluxes in satellite measurements during substorms. A study by Hayakawa et al. (1992) focused on the polarization of the Pc1 and IPDP events and noted an increase in AE index within a time interval of 2 hr prior to all IPDP events observed, indicating the association of these waves with substorms. Yahnina et al. (2003) showed that IPDP events were preceded by the enhancement of energetic proton fluxes (~ 100 keV) and were thus attributed to substorm activity. Clilverd et al. (2015) studied an electron precipitation event associated with rising tone EMIC waves on the ground and showed their association with substorm injection based on AE index and duskward drifting proton precipitation observed by Polar Operational Environmental Satellites (POES). However, the magnetosphere was compressed due to high solar wind dynamic pressure during their event. Furthermore, the event was followed by a moderate/large geomagnetic storm, indicating that it occurred during the onset of the storm.

Several satellite-based studies also attribute EMIC wave occurrence to substorms. Ishida et al. (1987) observed the occurrence of left-handed polarized Pc1 waves in the He band, accompanied by a decrease in the ambient magnetic field at geosynchronous orbit in the afternoon and evening local times and associate it with contemporaneous substorm activity. However, their study did not separate storm time from non-storm time substorms. They also suggested that Pc1 waves observed during substorm activity due to injection of energetic ions were limited to frequencies below the He cyclotron frequency. Blum et al. (2015) reported simultaneous EMIC wave activity on the ground and in space accompanied by energetic electron precipitation on two consecutive days in January 2013. The EMIC wave activity in their study was associated with solar wind pressure enhancements, followed by substorm injections and strong convection during the recovery of a geomagnetic storm. Kim et al. (2017) reported substorm-associated EMIC waves in geosynchronous satellite measurements in the premidnight sector. They showed strong waves in He band accompanied by a sudden decrease in the total magnetic field and a westward drift of the wave source, indicating substorm association. Their substorm-associated EMIC event followed another sudden impulse driven EMIC wave by ~ 4 hr. The solar wind conditions indicated that the magnetosphere was constantly compressed by a gradual increase in the dynamic pressure ($P_{\text{dyn}}=8$ nPa and still increasing) during this substorm-associated event.

He et al. (2017) recently reported a ~ 40 -nT magnetic dip event during substorm. They investigated the evolution of the magnetic dip at different locations of the duskside ring current and the related signatures, including EMIC wave generation, using multisatellite observations. However, their event occurred during the recovery phase of a moderate (SYM-H = -80 nT) geomagnetic storm.

It is well known that the anisotropic substorm-/storm-injected ions act as the primary source of free energy for driving EMIC waves. However, to our knowledge, no detailed study has been attempted to look into the EMIC waves that are excited solely due to the substorm-injected ions. Most of the previously reported substorm-associated EMIC events were either associated with a geomagnetic storm or occurred shortly after an abrupt increase in solar wind pressure on the dayside, or were in the high-pressure (> 3 nPa) interval after a sudden impulse. Here we focus on EMIC waves that are triggered solely due to substorm-injected ions, with no influence of geomagnetic storms or enhancements in solar wind dynamic pressure, ensuring that the source for EMIC wave free energy during nonstorm intervals is only the anisotropic ion injections on the nightside. The local plasma and magnetic field conditions that favor the EMIC wave generation are also looked at in detail.

The paper is organized as follows. In section 2 we describe the data set and the methodology used for this study. The solar wind conditions, the geosynchronous and ground measurements, and EMIC wave and ion distribution analysis during the active substorm interval is discussed in section 3. In section 4, the linear growth rate analysis and spectral properties of EMIC waves are presented. In section 5 we present summary and conclusions.

2. Data and Methodology

High-resolution (64 Hz) magnetic field data from the Electric and Magnetic Field Instrument Suite and Integrated Science (Kletzing et al., 2013) instrument on board National Aeronautics and Space Administration's Van Allen Probes are used to detect the EMIC waves. The Van Allen Probes mission (originally named Radiation Belt Storm Probes, RBSP) consists of twin spacecraft with identical instruments on board, following approximately the same trajectory at slightly different speeds. The two identical spacecraft (denoted as RBSP-A and RBSP-B) follow low inclination ($\sim 10^\circ$) elliptical orbits with a perigee of $1.1 R_E$ and apogee of $5.8 R_E$. Due to slightly different speeds, one probe overlaps the other about every 2.5 months. The energetic ions in the ring current are measured by the Energetic Particle, Composition, and Thermal Plasma suite (ECT) (Spence et al., 2013) on each Van Allen Probe spacecraft. Ions with energies 1 eV to ~ 51 keV are measured by the ECT/HOPE (Helium Oxygen Proton Electron) mass spectrometer instrument (Funsten et al., 2013) while energies from 50 keV to greater than ~ 1 MeV are measured by the ECT/Magnetic Electron Ion Spectrometer instrument (Blake et al., 2013). HOPE also measures the ion composition and gives separate flux information for protons, helium, and oxygen. We use pitch angle observations from HOPE and Magnetic Electron Ion Spectrometer to study the injection of ions during the substorm-associated EMIC events. This study also uses simultaneous electron density data obtained from the electric potential observed by the electric fields and waves instrument on Van Allen Probes spacecraft (Wygant et al., 2013).

Data from the Canadian Array for Realtime Investigations of Magnetic Activity (Mann et al., 2008) have been used to identify substorm onset signatures on the ground for correlation with the EMIC waves observed by the Van Allen Probes. The ground-based magnetometer arrays from Time History of Events and Macroscale Interactions during Substorms (Angelopoulos, 2008; Mende et al., 2008) are also surveyed to obtain substorm signatures on the ground. The two geosynchronous ($6.6 R_E$) satellite constellations, Geostationary Operational Environmental Satellite (GOES) and Los Alamos National Laboratory (LANL), are used to study the magnetic field and particle behavior at different MLTs. The magnetic field (MAG) and particle data from MAGnetospheric Electron Detector (MAGED) and MAGnetospheric Proton Detector (MAGPD) onboard GOES-13 and GOES-15 (Singer et al., 1996) are used to identify and characterize the substorm injection signatures at geosynchronous orbit. The particle flux data observed by Magnetospheric Plasma Analyzer and Synchronous Orbit Particle Analyzer (SOPA) (Reeves et al., 1996) on board six LANL satellites (LANL 1991-080, 1994-084, 97A, 01A, 02A, and 04A) are used to monitor substorm injection signatures. The solar wind parameters and geomagnetic indices are obtained from the OMNI database.

3. Observations

We present a detailed case study of a clear nonstorm, nonpressure pulse-driven EMIC wave event that occurred on 9 August 2015. Figure 1 presents the solar wind conditions before, during, and after the event on 9 August 2015. The interplanetary parameters are plotted for ± 6 hr before and after the event to gain an overall picture of the solar wind conditions in which the magnetosphere was immersed during the event. The panels from top to bottom are (a) interplanetary magnetic field \hat{z} component, (b) solar wind speed, (c) solar wind dynamic pressure (blue) and density (red), (d) AE, and (e) SYM-H indices. The vertical red line marks the start time of the EMIC event at $\sim 05:44$ UT observed by RBSP-A, which will be discussed in the next section. From the solar wind parameters, it is clear that there was no abrupt change in the dynamic pressure during or before the event. The SYM-H index remains nearly constant, around -10 nT, and provides no evidence for a geomagnetic storm. The AE index starts to increase around 03:00 UT, exhibits two intensification to ~ 500 nT at $\sim 04:48$ UT and 06:00 UT, and further increases to $\sim 1,300$ nT around 11:00 UT, much after the event. Solar wind speed remains close to 500 km/s throughout the interval. The z component of the interplanetary magnetic field, shown in the top panel, frequently changes direction from southward to northward during this interval, indicating possible periods of loading for ongoing substorm activity (McPherron, 1970).

Figure 2 shows the position in X - Y plane, in geocentric solar equatorial (GSE) coordinates, of the two GOES and six LANL geosynchronous satellites, and the Van Allen Probes during 05:00 to 07:00 UT on 9 August 2015. The locations of GOES-13 and GOES-15 are marked with pink and orange triangles, LANL satellites with colored squares, RBSP-A and RBSP-B with filled red and blue circles, respectively. GOES-15 was in the premidnight sector at $\sim 20:50$ MLT, while GOES-13 was located past midnight at $\sim 01:00$ MLT at 05:44 UT. The six LANL spacecraft were distributed through all local times. The two Van Allen Probes, RBSP-A and RBSP-B, were on their inbound trajectories and were located in the dusk sector. RBSP-A was at $\sim 18:06$ MLT and $L = 5.5$ at 05:44 UT during the onset of EMIC waves, and RBSP-B was at $\sim 19:12$ MLT and $L = 4.1$.

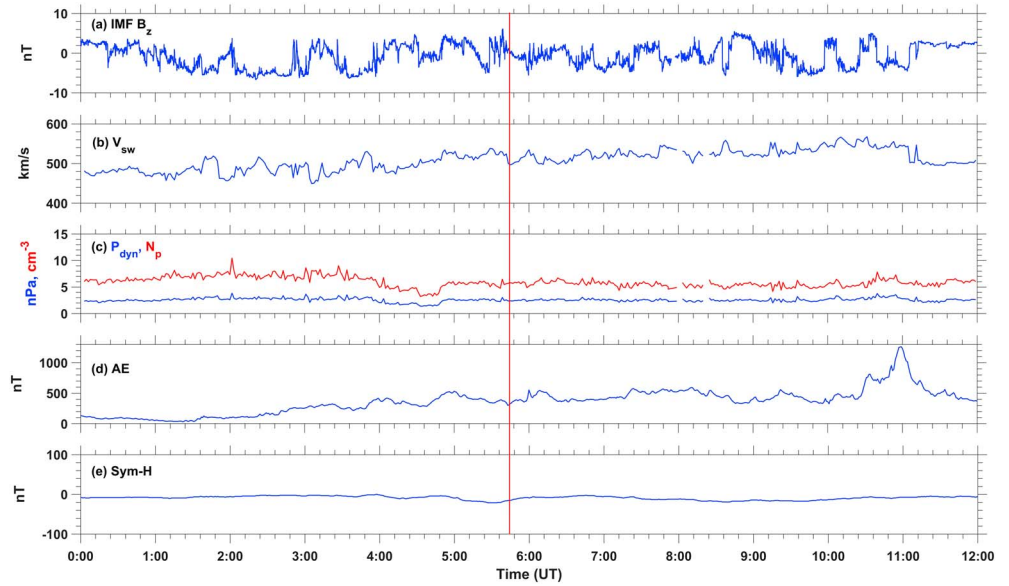


Figure 1. Summary plot for interplanetary parameters for 9 August 2015 from 00:00 to 12:00 UT. (a) IMF B_z , (b) solar wind speed, (c) solar wind dynamic pressure P_{dyn} (blue) and solar wind proton density N_p (red) and geomagnetic indices, (d) AE, and (e) SYM-H. The units are marked on the y axis. The red vertical line shows the start time of the EMIC wave activity observed at RBSP-A. IMF = interplanetary magnetic field; RBSP = Radiation Belt Storm Probes.

3.1. EMIC Waves and Particle Injections at Van Allen Probes

Figure 3 shows the local magnetic field behavior observed by RBSP-A on 9 August 2015. Figure 3a shows the dynamic spectra of the magnetic field, and Figures 3b–3d show the magnetic field components in spherical coordinates θ and ϕ and magnitude of the total magnetic field $|B|$, respectively. Here θ and ϕ are the latitude and longitude measured in GSE coordinates measured from the Sun-Earth line, with longitude increasing toward dusk. The plot is shown for the interval 05:00–07:00 UT. The white lines in Figure 3a show the cyclotron

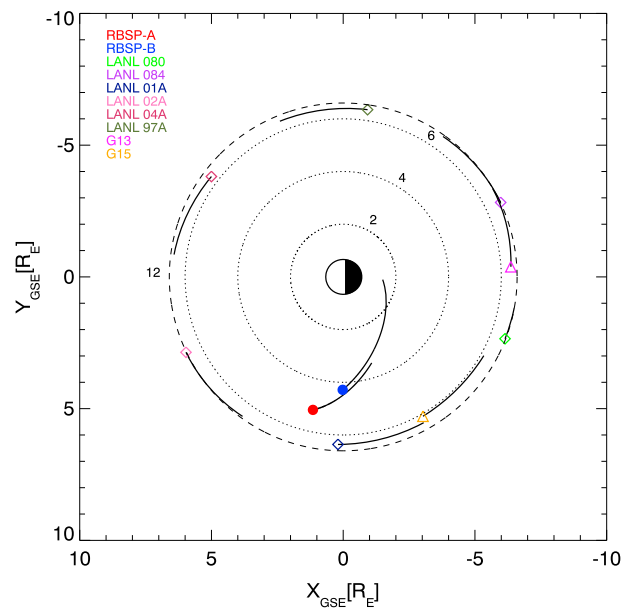


Figure 2. Trajectories of RBSP-A and RBSP-B (circles), six LANL spacecraft (squares) and GOES-13 and GOES-15 (triangles) during 09 August 2015 for the period from 05:00 to 07:00 UT in the X-Y plane (GSE coordinates). The L shells are marked with dotted lines, and the geosynchronous orbit at $6.6 R_E$ is marked with dashed line. GSE = geocentric solar equatorial. RBSP = Radiation Belt Storm Probes; GOES = Geostationary Operational Environmental Satellite; LANL = Los Alamos National Laboratory.

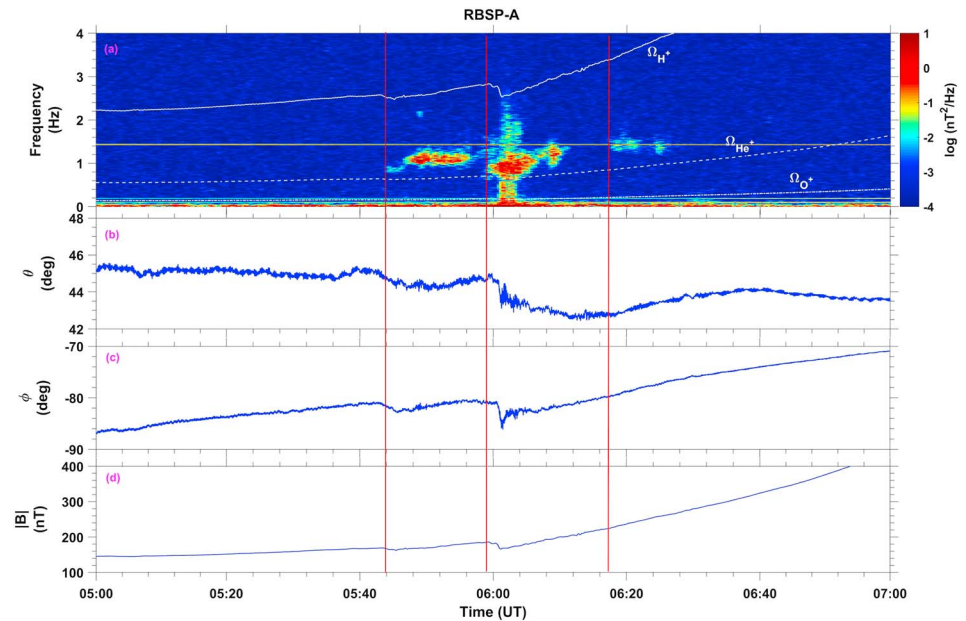


Figure 3. (a) The dynamic spectra of magnetic field B_x component observed by RBSP-A on 9 August 2015. White lines indicate the gyrofrequencies for proton (solid), helium (dashed), and oxygen (dash-dotted line). EMIC wave signatures are seen at frequencies in H band between proton and helium gyrofrequencies. The second patch of EMIC wave is seen to spread below Ω_{He} into the helium band. (b–d) The time variation of the magnetic field components in spherical coordinates θ , ϕ , and magnitude of magnetic field $|B|$ as obtained from RBSP-A. The red vertical lines indicate the start time of each patch of the EMIC wave activity in Figure 3a. RBSP = Radiation Belt Storm Probes; EMIC = electromagnetic ion cyclotron.

frequencies of proton (solid), helium (dashed), and oxygen (dash-dotted line). EMIC waves are seen to occur in the proton branch in three patches with onsets at $\sim 05:43:50$ UT, $\sim 05:58:52$ UT, and $\sim 06:17:40$ UT, respectively. The second patch of EMIC wave is seen to spread below Ω_{He} into the helium band. However, this seems to be a broadband signal caused by the sharp gradient in magnetic field, rather than a helium band EMIC wave. The total field strength diminishes at the start of the EMIC wave activity for the first two patches of EMIC waves. The third (weaker) patch of the EMIC wave activity does not show any clear field decrease signature. This could be because the satellite is closer to the Earth and/or because the field decrease is very small or negligible. A polarization analysis for the waves shown here confirmed that they were left-hand polarized EMIC waves (not shown in the paper). RBSP-B was in its inbound trajectory at $L < 4$, $\sim 01:18$ hr ahead of RBSP-A, and did not observe any EMIC wave activity during this period.

Based on past work, we expect the ion populations to exhibit enhanced anisotropies when the EMIC waves are observed. Figure 4 displays pitch angle distributions (PAD) for the top 12 proton energy channels (15.9 to 51.8 keV) observed by the HOPE instrument on board RBSP-A. The energy decreases from top to bottom and left to right as indicated on each panel. Sudden increases seen in the proton flux at $\sim 05:38:30$ UT, $\sim 05:56:32$ UT, and $\sim 06:11:40$ UT indicate clear signatures of proton injection across all energies. For the first injection, the proton flux increases are not very clear in the top two energy channels, 51.8 keV and 46.5 keV. The first injection begins when 41.7-keV protons with 90° pitch angles begin arriving at 05:38:30 UT. At 15.9 keV, protons with 90° pitch angles only begin to arrive at 05:45 UT. Protons with lower local pitch angles arrive even later. This is due to the different drift periods of the different pitch angle particles. The delay in arrival times between the highest (90°) and lowest pitch angle particles is approximately between ~ 2 and 6 min for all energies for the first injection signature. The second injection begins when 41.7-keV protons with 90° pitch angles begin to arrive at 05:56:32 UT. At $\sim 06:04$ UT, enhanced fluxes begin to arrive at 15.9 keV with 90° pitch angles. Lower pitch angles arrive later than 90° pitch angle particles at all energies. Finally, the third injection is very dispersed. At 51.8 keV, protons with 90° pitch angles begin arriving at 06:11:40 UT, and at 21.9 keV enhanced fluxes appear near $\sim 06:37$ UT. The flux from this dispersive injection seems to have merged with the flux from the second injection at lower energies ($E < 24$ keV). We interpret the delays at which particles with lower pitch angles and energies arrive as evidence for proton injections at some distance away from the observing

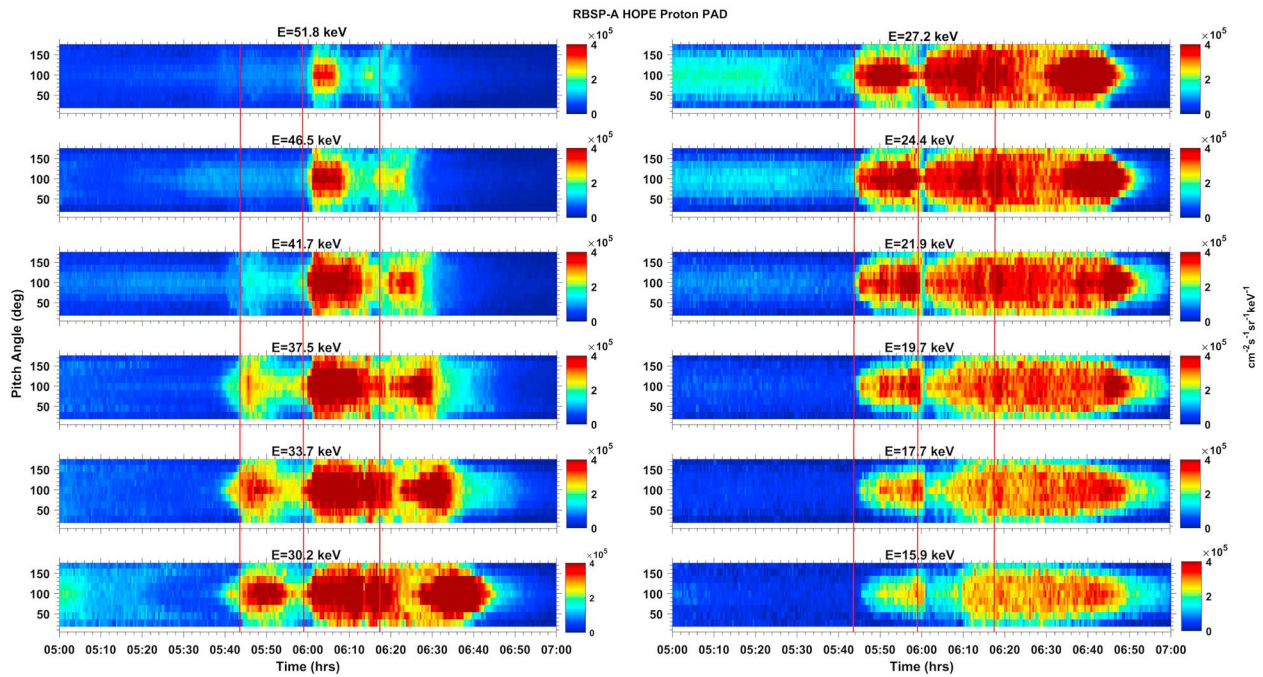


Figure 4. The pitch angle distributions (PADs) of 15.9- to 51.8-keV protons as observed by HOPE instrument on board RBSP-A. The energy is highest at the top left and decreases toward the right bottom. The red vertical lines indicate the start time of each patch of the EMIC wave activity seen in Figure 3. RBSP = Radiation Belt Storm Probes; HOPE = Helium Oxygen Proton Electron.

spacecraft. Based on the longer time lags for the third injection, it is clear that the first two injections occurred nearby while the third injection occurred further away and/or could be a drift echo. Vertical lines in the figure indicate the times when the EMIC wave activity identified in Figure 3 began. The onset of the EMIC waves at $\sim 05:43:50$ UT (see Figure 3) is slightly delayed as compared to the time when the ion injections arrive first ($\sim 05:38:30$ UT).

Whether or not the injections resulted in enhanced plasma anisotropies and what factors triggered EMIC wave onset can be determined by inspecting Figure 5, which repeats the plot showing wave activity (a) for easy comparison and adds panels showing (b) plasma anisotropies T_{\perp}/T_{\parallel} for protons, helium, and oxygen ions, (c) cold ion densities from electric fields and wave potential measurements, (d) total hot (>30 eV) ion densities, (e) densities by species, and (f) density ratios during the interval of interest. There are indeed enhanced anisotropies at $05:40:30$ UT ($T_{\perp,p}/T_{\parallel,p}=1.8$) and at $06:00:30$ UT ($T_{\perp,p}/T_{\parallel,p}=1.78$) just prior to the first two enhancements in wave activity (red vertical lines) and particle injections. As can be seen by inspection of Figure 4, these enhancements result from the arrival of energetic particles with 90° pitch angles. The anisotropies disappear quickly with the arrival of particles with lower pitch angles. At least in the case of the first injection, the anisotropies do not disappear in response to wave activity. Comparison of Figures 5a and 5b shows that the proton anisotropy has already diminished to ambient levels of $T_{\perp,p}/T_{\parallel,p} \simeq 1.45$ by $05:43:50$ UT, whereas wave activity intensified substantially only after $\sim 05:46$ UT.

If enhanced ion anisotropies are not the cause of the wave activities, there must be some other cause. The answer lies in the enhanced densities associated with the particle injections. While Figure 5c shows no enhancement in the cold plasma density, Figure 5d shows clear hot plasma enhancements at the times of the first two injections. Figures 5e and 5f demonstrate that the injections are primarily composed of protons. A drop in the oxygen to proton density ratio is seen at the onset of the EMIC waves that is due to the increase in hot proton density as shown in Figure 5e. Lower hot oxygen density ratios are also known to lower the EMIC wave growth rate as per the linear theory. For the second EMIC wave onset, the hot helium density (Figure 5e) and thereby helium to proton ratio (Figure 5f) increases. Cold plasma densities increase for the third event, while hot plasma densities remain high, anisotropy conditions remain the same, and no further specific changes are noted.

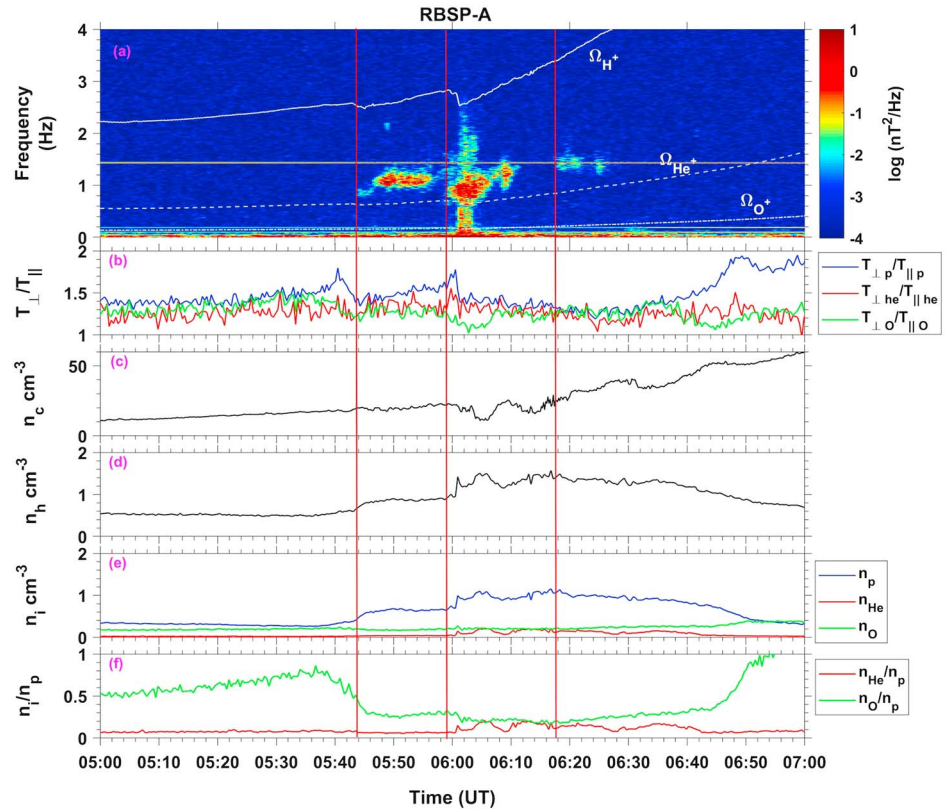


Figure 5. The ion plasma parameters obtained from the HOPE instrument are shown. (a) Dynamic spectra of wave magnetic field (same as in Figure 3a) (b) Temperature anisotropy T_{\perp}/T_{\parallel} for protons (blue), helium (red), and oxygen (green). (c) Cold plasma density calculated from the spacecraft potential obtained from EFW instrument on RBSP-A. (d) Total hot ion density, (e) hot ion densities of proton (blue), helium (red), and oxygen (green), and (f) ratio of density of helium (red) and oxygen (green) to protons. The red vertical lines indicate the start time of each patch of the EMIC wave activity. EFW = electric fields and waves; HOPE = Helium Oxygen Proton Electron; RBSP = Radiation Belt Storm Probes.

In the case of second injection, the ion populations exhibit enhanced anisotropies as the EMIC waves are observed. The anisotropies seem to reduce after the wave activity onset at 05:58:52 UT. As EMIC waves are known to diffuse ions in pitch angle thereby isotropizing them, the presence of EMIC waves could also be a reason for the reduction in temperature anisotropy in this case. To estimate and quantify whether the excitation of EMIC waves relax the temperature anisotropy in this case, we calculate the pitch angle diffusion time for protons (Kennel & Petschek, 1966; Remya et al., 2015; Tsurutani & Lakhina, 1997). We assume that the duration of EMIC wave packet interacting with protons is about ~ 45 s, approximate time interval during which the anisotropy was reduced. The pitch angle diffusion time was found to be between ~ 10 and 20 ms depending on the energy of the particle. Hence, the immediate reduction in proton temperature anisotropy occurring close to $\sim 06:00$ UT could also be due to the pitch angle diffusion of protons by the EMIC waves or due to combined effect of EMIC wave scattering and the arrival of lower pitch angle particles.

Table 1 shows the time sequence of events as it occurred. The columns show the timings at which the injection first arrived at the satellite, the time of peak temperature anisotropy and the peak value of $T_{\perp p}/T_{\parallel p}$, start time of flux rise, EMIC wave onset, and the time of maximum flux as observed by the satellite. From the time sequence, it is easier to understand what factors/parameters are most important for the onset of EMIC wave activity. It should be noted that the EMIC wave onsets do not directly correspond to the initial arrival times of the energetic particles or to the maximum temperature anisotropy. On the other hand, the time of flux rise closely corresponds to the onset of first two patches of EMIC waves. This is also clear from the PAD of protons shown in Figure 4. The EMIC wave onsets correspond to the increased proton flux levels, where the particles are less anisotropic.

Table 1
Time Sequences

Injection first arrives	Exact time when			
	Anisotropy peaks (peak $T_{\perp p}/T_{\parallel p}$)	Hot ion density rise	Wave activity onset	Hot ion density peaks
05:38:30	05:40:29 (1.798)	05:43:30	05:43:50	05:45:10
05:56:32	06:00:30 (1.779)	05:58:35	05:58:52	06:00:51
06:11:40	–	–	06:17:40	06:18:21

We can strengthen our understanding of the relationship between the wave power, magnetic field strength, and particle fluxes by cross-correlating observations during this interval. Figure 6 shows the cross correlation, in time, of wave power with magnetic field and proton flux to further demonstrate that the arrival of substorm-injected ions triggers EMIC wave onset. Figure 6 shows (a) magnetic field magnitude, (b) EMIC wave power, (c) spin-averaged proton flux, (d) cross correlation between magnetic field and wave power, and (e) cross correlation between proton flux and wave power. Note that the highest-energy particle fluxes exhibit the sharpest peak near 0 s lag. Maximum correlation for the magnetic field also occurs at zero lag. This further validates our proposition that the arrival of substorm-injected ions along with the dip in the magnetic field favored EMIC wave onset.

3.2. Geosynchronous and Ground Measurements

In addition to the wave and particle observations from RBSP-A, magnetic field measurements from ground magnetometers and GOES satellites and particle measurements from GOES and LANL satellites are studied to understand the field and particle behavior at geosynchronous orbits. Figure 7 shows the magnetic field and particle flux observations from the two GOES spacecraft and the magnetic field behavior observed on the ground during the interval under study. Figure 7a displays the geosynchronous magnetic field from

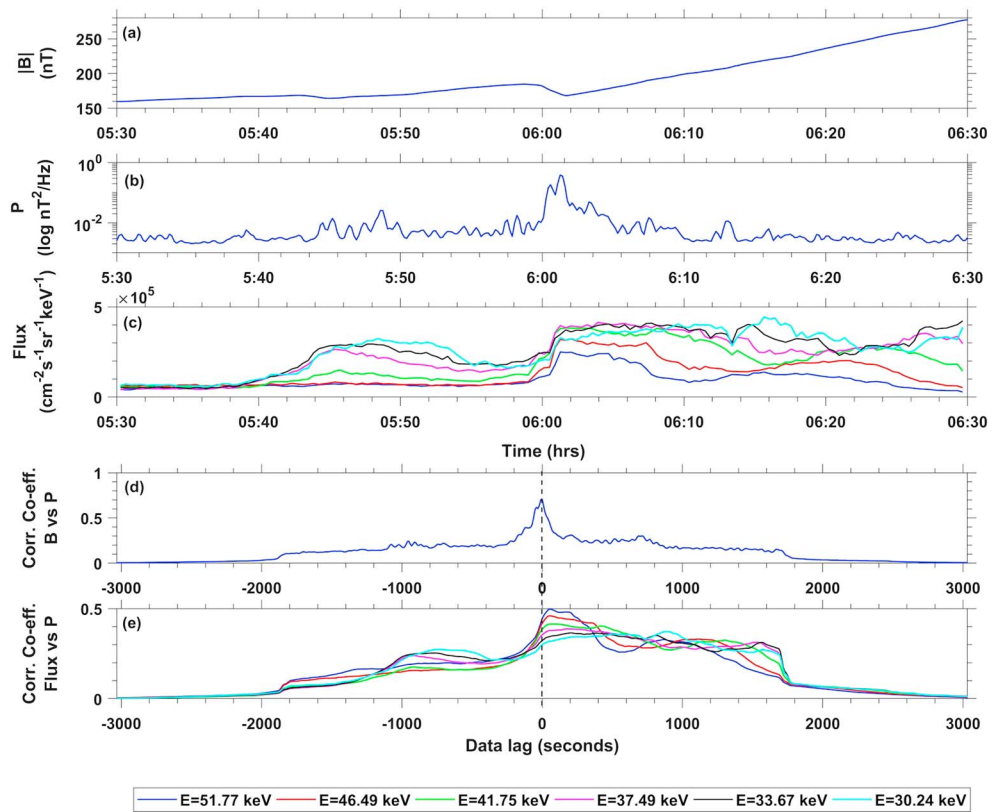


Figure 6. (a) Magnetic field magnitude $|B|$, (b) EMIC wave power P , (c) spin-averaged proton flux, (d) cross correlation between magnetic field and wave power, and (e) cross correlation between proton flux and wave power. EMIC = electromagnetic ion cyclotron.

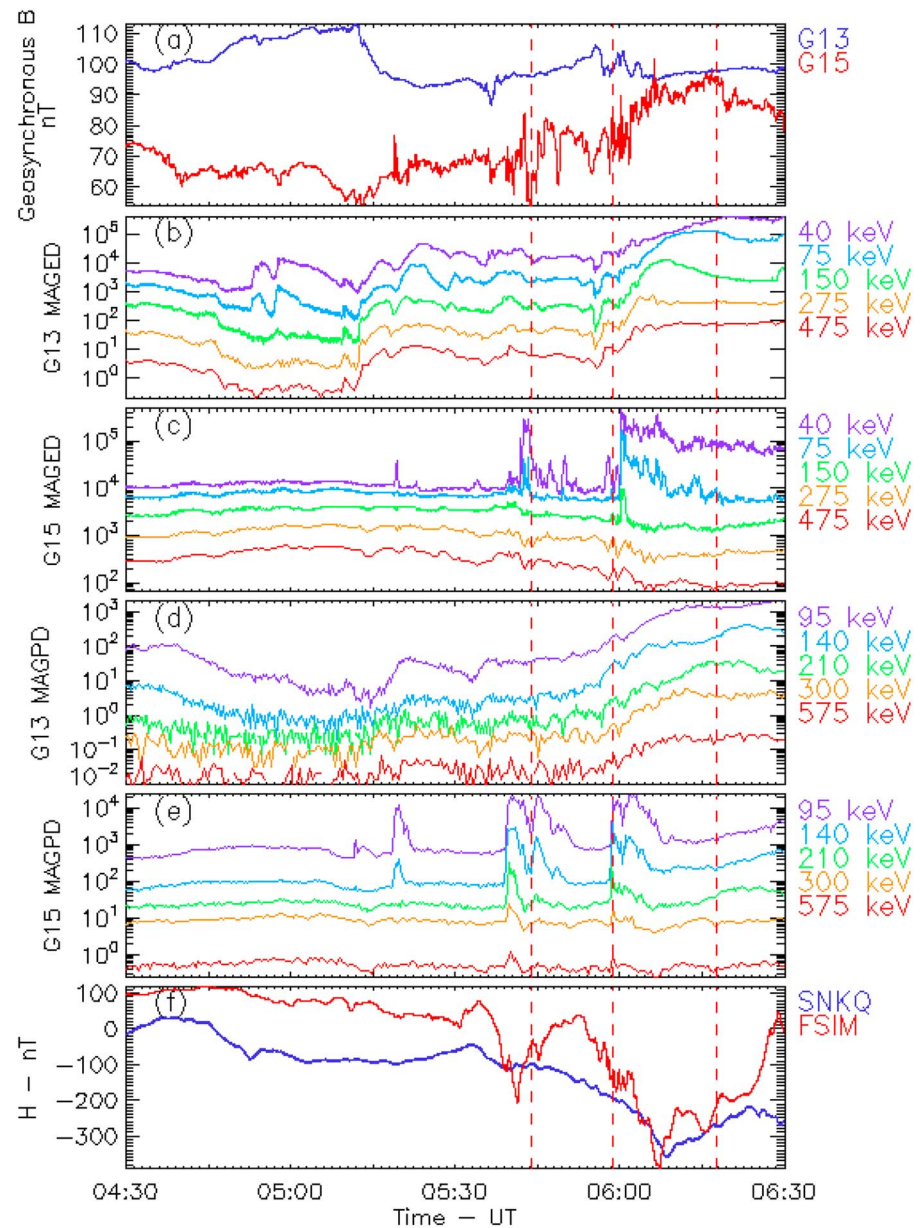


Figure 7. (a) The magnetic field magnitude (in nanotesla) at the geosynchronous orbits for GOES-13 (blue) and GOES-15 (red). The near-equatorial electron flux for energies 40–500 keV are shown for (b) GOES-13 and (c) GOES-15. Different energies are marked using different colors as indicated outside the panels, and the fluxes are in units of $e/(cm^2 sr s keV)$. The near-equatorial flux ($p/(cm^2 sr s keV)$) for 95- to 575-keV protons are plotted (d) for GOES-13 and (e) for GOES-15, respectively. (f) The magnetometer responses from two ground stations Sanikiluaq (SNKQ) (blue), conjugate to GOES-13, and Fort Simpson (FSIM) (red), conjugate to GOES-15. GOES = Geostationary Operational Environmental Satellite.

GOES-13 (blue) and GOES-15 (red). Figures 7b and 7c show the near-equatorial electron flux from GOES-13 and GOES-15, respectively. The near-equatorial proton flux observed by GOES-13 and GOES-15 are shown in Figures 7d and 7e, respectively. Different energies are marked with different colors as labeled outside each panel. GOES-15 observed a sharp transient increase in proton fluxes at $\sim 05:17:30$ UT (Figure 7e) visible clearly for lower energy channels ($E < 140$ keV). The same spacecraft observed a second and third rises in proton fluxes at $\sim 05:38:00$ and $\sim 05:57:45$ UT at all energies. Each of these flux rises show a double peaked behavior. This suggests possible successive nightside injections. While the first injection signature was not seen by RBSP-A, the second and third injections seem to have reached RBSP-A almost simultaneously, which may have triggered the EMIC waves. It is surprising to note that GOES-15 also observes an abrupt rise in electron fluxes (Figure 7c) at $\sim 05:42$ UT and $\sim 06:00$ UT at all energies, each following proton injections by approxi-

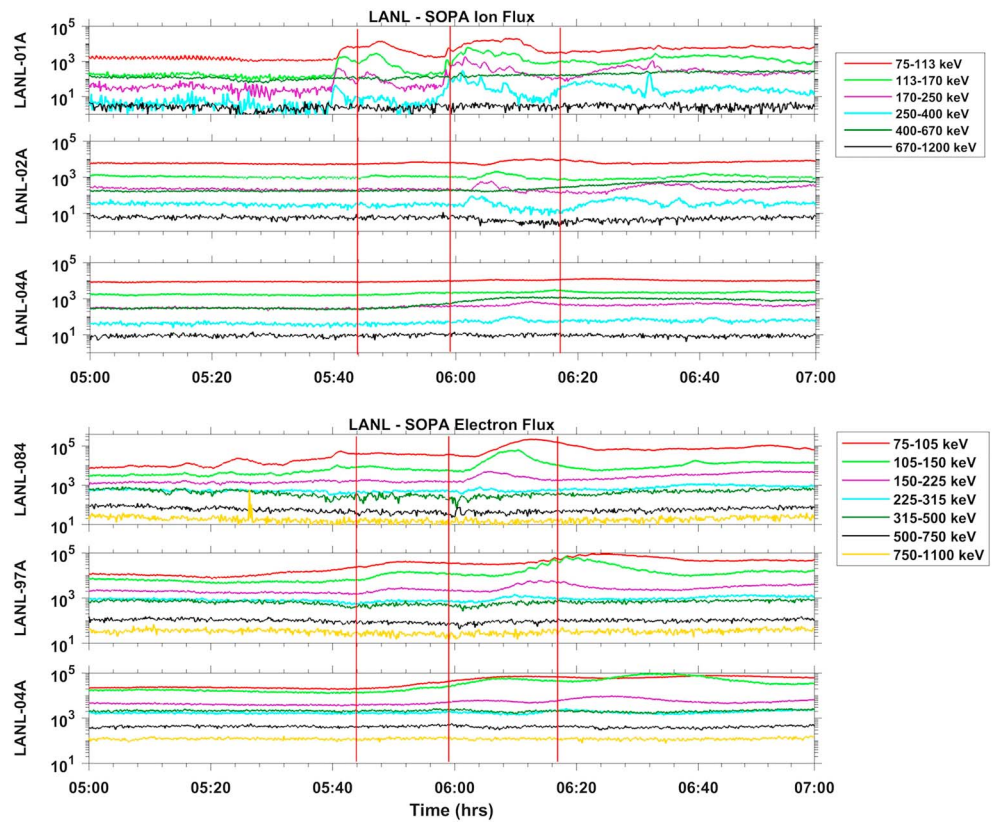


Figure 8. LANL SOPA ion and electron fluxes from 75 keV to ~1.2 MeV from different LANL geosynchronous spacecraft during 05:00–07:00 UT on 9 August 2015. The panels from top to bottom show ion (electron) fluxes for LANL spacecraft distributed westward (eastward) in local time away from midnight. Dispersed injection signatures are visible in the ions and electrons during the interval. LANL = Los Alamos National Laboratory; SOPA = Synchronous Orbit Particle Analyzer.

mately ~2–3 min. Since GOES-15 observes near simultaneous dispersionless injections of both protons and electrons, the location of the injections must be close to the location of GOES-15 at ~20:00 MLT. Past studies show that substorm onsets that are associated with injections predominantly occur just prior to midnight at 23:00 MLT (Frey et al., 2004; Frey & Mende, 2006). However, the reports also suggest rare occurrences of premidnight/postmidnight injections.

At GOES-13 the magnetic field strength decreases at ~05:12 UT (Figure 7a). This corresponds to the increase in electron flux at all energies (Figure 7b) also observed by GOES-13. The flux increase is dispersive, higher-energy fluxes increase first ($E = 475$ -keV peaks at ~05:21 UT) followed by lower energies ($E = 40$ -keV peaks at ~05:25 UT). The pressure associated with the eastward drifting injected electrons was found to balance the pressure associated with the decrease in the magnetic field. The expected corresponding proton flux increase was not seen by GOES-13 because GOES-13 was located postmidnight and protons injected on the nightside drift westward. There is no obvious decrease in the magnetic field strength in GOES-15 due to drifting ions. The GOES-15 magnetic field power spectrum (see Figure 11) for the study interval does not indicate the presence of EMIC waves. However, there was a large ULF wave activity spanning the entire interval, which might have also possibly masked EMIC wave activity, if any were present.

To confirm the substorm occurrence and to appropriately identify its injection location, we inspect ground magnetometer responses. Figure 7f shows the H component of the magnetic field measured by two ground-based magnetometers. Figure 7f shows the H component of the magnetic field measured by two ground-based magnetometers. The plots are for the ground stations Sanikiluaq (SNKQ), which is conjugate to GOES-13, and Fort Simpson (FSIM), which conjugate to GOES-15. There is a clear substorm initiation around 05:33 UT at SNKQ (blue) characterized by a negative H -bay. The substorm is quite large reaching 400 nT at 06:10 UT. At FSIM (red), which is about 3 hr of MLT away from SNKQ and conjugate to GOES-15, there are two substorms: one beginning at ~05:34 UT and one at ~05:52 UT, respectively. These onsets correspond to the

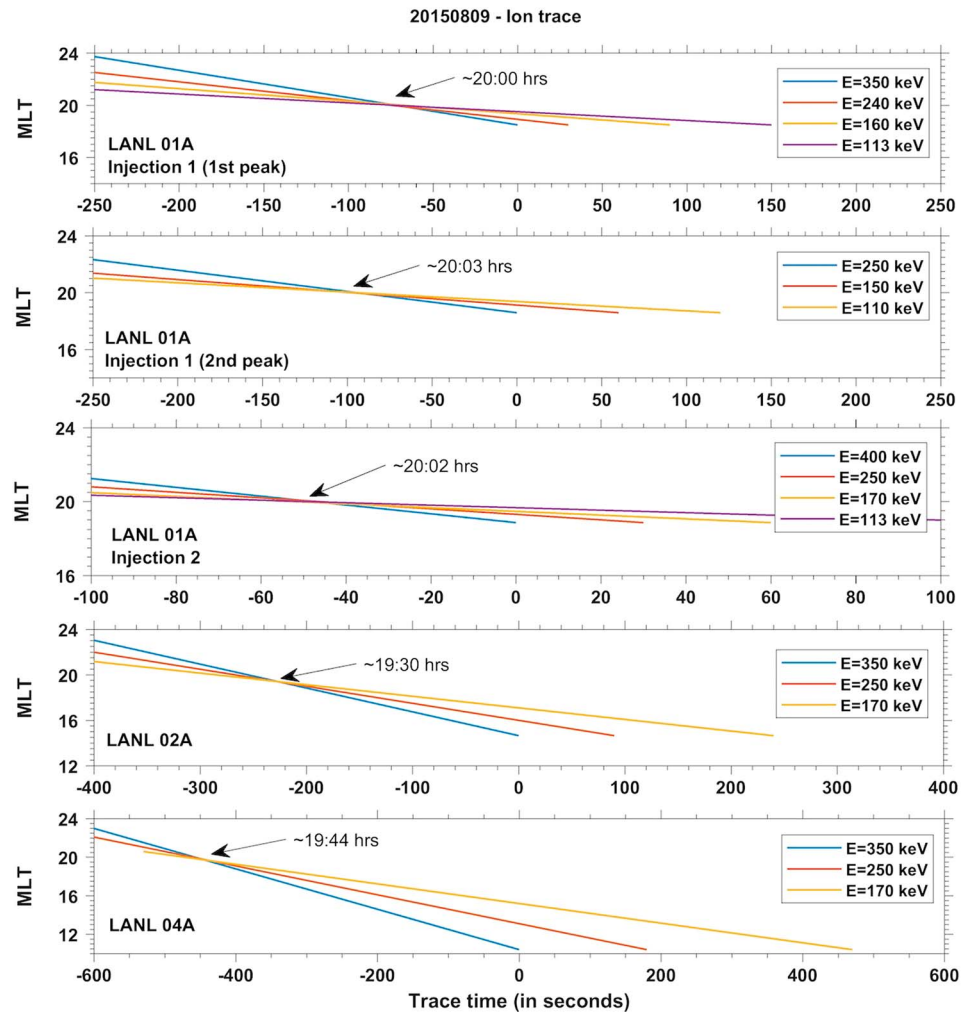


Figure 9. Trajectories of ions traced back in a dipole field model to locate the injection location using arrival times of dispersive injection signatures observed by various LANL spacecraft. The injection location is traced to be between 19:30 and 20:03 MLT. LANL = Los Alamos National Laboratory; MLT = magnetic local time.

two nondispersive flux rises observed at GOES-15. While the first substorm was not very dramatic, the second substorm injection was quite large and the electrons from this injection drifted eastward and made their way to GOES-13 where we observe a dispersed electron flux rise. The magnetometer response from other nearby ground stations (not shown here) reveals that the substorms initiated at location close to GOES-15.

Figure 8 shows ion and electron flux data observed by LANL SOPA for different energy channels. The dispersive injection of protons and electrons is measured at different local times depending on the location of the spacecraft (see Figure 2), with electrons drifting around to the dawn and ions to the dusk. The fluxes are shown only for spacecraft that see either an ion or electron flux rise. The panels show SOPA ion fluxes for LANL-01A, LANL-02A, and LANL-04A and SOPA electron fluxes for 1994-084, LANL-97A, and LANL-04A from top to bottom. There is a clear increase in ion flux at energies $E = 75\text{--}400$ keV observed by LANL-01A (top panel) at 05:40 UT and another peak at 05:46 UT. A second flux increase is observed at $\sim 05:59$ UT by the same spacecraft. The dispersion in the flux increase is very small, which further confirms our speculation that the substorm injection occurred close to $\sim 20:00$ MLT and arrived rapidly at LANL-01A at $\sim 18:40$ MLT. The injection signatures become more dispersive traveling further westward as observed by LANL-02A and LANL-04A. Similarly, dispersive electron injections are observed by 1994-084 becoming more dispersed eastward moving down through the panels.

To further validate our speculation on the location of substorm injection, we use the arrival times of the dispersed injection signatures observed by LANL and GOES to trace back the particles in a dipole field model

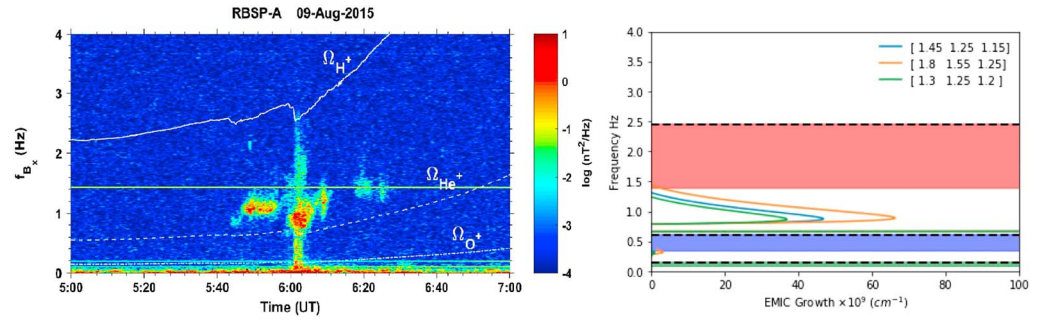


Figure 10. The magnetic field power spectral density for the EMIC waves observed by RBSP-A (left-hand panel) and the calculated linear theory convective growth rates (in cm^{-1}) for three different sets of ion anisotropy values (right-hand panel). The three set of values correspond to the anisotropy values measured at the time of three EMIC wave onsets in Figure 3. The legend vector represents the temperature anisotropy for the three species H, He, and O, respectively. The black dashed lines are the calculated ion gyrofrequencies and the colored bands below them are the stop bands. EMIC = electromagnetic ion cyclotron; RBSP = Radiation Belt Storm Probes.

(Reeves et al., 1991; Turner et al., 2017). We assume particles to be 90° pitch angle and that the drift speed of particles is due to the gradient in the magnetic field. The magnetic field at the location of the spacecraft is calculated using a dipole assumption and drift speed, for different energy ions/electrons are obtained. The observed arrival times of different energy ion/electron peaks are then used to estimate their injection location by tracing back the respective drift paths in time. As a validation check for dipole model, we also used Tsyganenko and Sitnov's (2005) model to calculate drift paths of the particles observed at geostationary orbits and trace their trajectories to their injection location/s. The results from both the models are found to be consistent with each other. Figure 9 shows results of particle tracing for different injection signatures observed at different LANL spacecraft using dipole magnetic field model. The intersection point of the curves from different energies (marked in different colors) in Figure 9 gives an estimate of injection location in MLT. Any small spread seen at the convergence points is an estimate of the error in the analysis for that set of energy values, injection arrival times, and field model used. Dispersive ion signatures from LANL were traced back to 19:30–20:03 MLT as was speculated as the location of our substorm event from ground and GOES measurements. Dispersed electron signatures observed at spacecraft eastward of midnight trace to location $\sim 20:40$ MLT (not shown). As the electrons (ions) drift eastward (westward) in the magnetosphere, the location traced by them should provide an estimate of the eastward (westward) boundary of the injection location in MLT. Hence, the injection we observe should have a westward boundary around $\sim 19:30$ MLT and an eastward boundary at $\sim 20:40$ MLT, estimating the center of the injection to be around $\sim 20:00$ MLT. This further supports our speculation that the substorm injection location was close to Van Allen Probes.

4. EMIC Instability Analysis

To evaluate the EMIC wave instability quantitatively, we examine the growth rates of the EMIC instability using the observed plasma and magnetic field parameters. The linear convective growth rate S of an instability is given by the ratio of its temporal growth rate (γ) to its group velocity V_g . Following the linear theory calculations from Kozyra et al. (1984), the convective growth rate for the EMIC wave instability is obtained as

$$S = \gamma / V_g = \sum_l \frac{\eta_{lw} \sqrt{\pi}}{M_l^2 \alpha_{\parallel,l}} [(A_l + 1)(1 - M_l X) - 1] \exp \left\{ \frac{-\eta_{lw} (M_l X - 1)^2}{M_l \beta_{lw} X^2} \left/ \left[\frac{1 + \delta}{1 - X} + \sum_j \frac{(\eta_{jw} + \eta_{jc}) M_j}{1 - M_j X} \right] \right. \right\} \left\{ 2X^2 \left[\frac{1 + \delta}{1 - X} + \sum_j (\eta_{jw} + \eta_{jc}) \frac{M_j}{1 - M_j X} \right] \right\}^{-1} \quad (1)$$

In the above equation, summations over l include all ions and those over j include only ions heavier than H^+ . X is the ratio of real frequency ω_r of the wave to proton cyclotron frequency Ω_p ($X = \omega_r / \Omega_p$) and $\eta_{jw(c)} = M_j (\omega_{pjw(c)}^2 / \omega_{ppw}^2)$. Here $M_l = m_l / z_l m_p$ is the ion mass ratio, $\omega_{plw(c)}$ is the plasma frequency of the species l and the subscripts $w(c)$ indicate warm (cold) plasma components. The temperature anisotropy of particles is

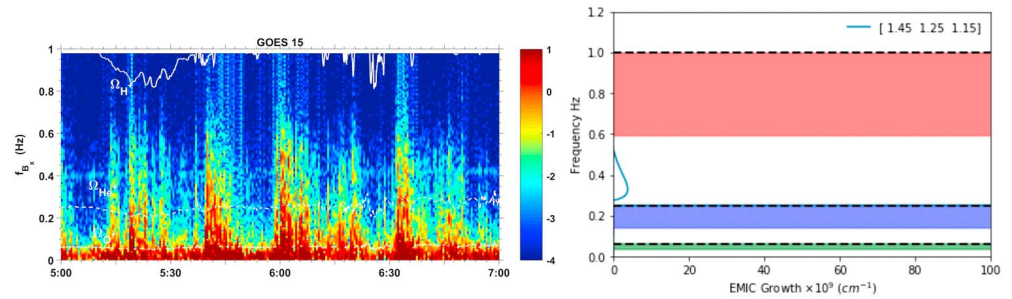


Figure 11. The magnetic field power spectral density observed by GOES-15 (left-hand panel) and the calculated linear theory convective growth rates (in cm^{-1}) for observed GOES-15 parameters (right-hand panel). The legend shows the assumed temperature anisotropy for the three species H, He, and O, respectively. The black dashed lines are the calculated ion gyrofrequencies, and the colored bands below them are the stop bands. EMIC = electromagnetic ion cyclotron; GOES = Geostationary Operational Environmental Satellite.

defined as $A_l = (T_{\perp,l}/T_{\parallel,l}) - 1$; $T_{\perp,l}$ and $T_{\parallel,l}$ are the temperatures measured perpendicular and parallel to the background magnetic field B_0 ; and $\alpha_{\parallel,l}$ is the parallel thermal velocity of the energetic species l . The plasma beta $\beta_{lw} = 8\pi n_{lw} k_B T_{\parallel,l} / B_0^2$, k_B is the Boltzmann's constant, n_{lw} is the density of the warm plasma component l , and $\delta = \omega_{ppc}^2 / \omega_{ppw}^2$.

The EMIC wave convective growth rate is calculated using the observed parameters of the ambient magnetic field, temperature anisotropy and density of hot protons, helium, and oxygen, and cold plasma number density at RBSP-A. Figure 10 shows the observed EMIC wave power spectrum in the left-hand panel and the calculated linear convective growth rates in the right-hand panel. The various growth curves are for three different ion temperature anisotropy values as shown in the legend vector for proton, helium, and oxygen. The blue, orange, and green curves correspond to the anisotropy values observed at the start of the three EMIC wave patches seen on the left panel. The black dashed lines indicate the theoretical ion gyrofrequencies and the colored bands below them mark the stop bands. As observed, the power spectral density of the magnetic field shows intense EMIC waves in the hydrogen band and the second wave patch has maximum wave power, which is consistent with the linear theory. The above linear theory analysis demonstrates that the EMIC waves are likely triggered by the enhancement of hot ion densities and reduced magnetic field.

The EMIC wave linear growth rates were also calculated for the observed parameters at GOES-15, and the results are shown in Figure 11. The left-hand panel shows the spectrogram of the GOES-15 magnetic field, and the right-hand panel shows the calculated linear growth rates for the observed parameters at geosynchronous location. The spectrogram shows intense ULF wave activity throughout the interval of the study. For linear theory calculations, since GOES measurements do not provide information about hot proton temperature anisotropy, we assumed maximum anisotropy values observed by RBSP-A. Hot ion composition are assumed as approximate values at geosynchronous orbits. Magnetic field magnitude and hot ion temperature used in the calculation are obtained from GOES-15 observations. It was seen that, for the parameters at GOES-15, linear theory suggests small-amplitude EMIC growth rate, which is around 9 times less than that expected at RBSP-A location. These small-amplitude EMIC waves are probably masked by the intense ULF wave activity observed at GOES-15 during the study interval.

5. Summary and Discussion

EMIC waves can pitch angle scatter ring current ions as well as relativistic electrons into their respective loss cones, thereby playing a major role in particle loss processes in the Earth's magnetosphere. Due to their vital role on radiation belt dynamics, it is extremely important to understand when, where, and under what conditions these waves grow or do not grow. The present study shows that substorm-injected ions can generate EMIC waves. There are very few previous studies that report EMIC waves in association with substorms. However, they have not separated the substorm events from periods of geomagnetic storms or pressure enhancements. This has led to a situation where it can be difficult to interpret the actual cause of the observed EMIC wave growth, for instance, whether it is due to the prestorm magnetospheric compression, strong injections, or solar wind pressure pulses during geomagnetic storms, or quiet time dayside compressions in response to high solar wind dynamic pressure. Our study looks into EMIC waves that are triggered

solely by substorm-injected ions. The current study focuses on the detailed analysis of one such nonstorm, nonpressure pulse, and duskside event that was possibly triggered due to substorm-injected anisotropic ions. A detailed statistical study on such events based on their local time, ion PAD, and magnetic field behavior will be addressed in a future work.

The EMIC wave event associated with a substorm injection on 9 August 2015 occurred at approximately ~05:44 UT with two other successive injection signatures, each associated with an EMIC wave onset. The event was observed by Van Allen Probe A at ~18:06 MLT and $L \approx 5.5$. For the first two strong injections, dips in the magnetic field due to the duskward drift of an ion plasma injection are evident. A very small dispersion in energy of the ion fluxes observed by HOPE instrument on board RBSP-A indicates that the injections occurred at locations close to the Van Allen Probe location. Geosynchronous and ground magnetometer measurements reveal that a substorm initiated at ~20:00 MLT, close to the location of GOES-15. The arrival time of particles of different energies at multiple geosynchronous satellites (GOES and LANL) is used to trace back the particles to their injection location. Assuming a dipolar magnetospheric magnetic field of Earth, all particles tend to originate at a location close to ~20:00 MLT.

This study supports the role of substorm-injected ions for the growth of EMIC waves. The maximum theoretical growth rates calculated using the observed field and plasma parameters matches spectacularly with the frequency where we observe the maximum EMIC wave power. In other words, the arrival of substorm ion injections produces magnetic field and plasma conditions that favor EMIC wave growth. The onsets of EMIC waves in the study are clearly associated with the increase in hot anisotropic ion density. A dip in the magnetic field is observed, also associated with the arrival of the ion flux. It is interesting to note that the EMIC wave activity in the present study more closely corresponds to the enhanced hot ion densities than to the initial arrival of energetic particles or to the peak anisotropies.

Substorm ion injections provided favorable ion and the magnetic field conditions to cause the observed EMIC growth at RBSP-A. In contrast, GOES 15, which was also in the path of the substorm injection, did not observe EMIC activity. Our estimates of the expected growth at GOES suggest that the EMIC wave would not have been large enough to be observed above the ULF broadband activity seen in the EMIC frequency range. This suggests that substorm-driven EMIC waves may not occur along the entire path of the substorm injection and thus may have a very limited extent of influence over radiation belt electrons. Further work is needed to determine the size of the EMIC active region due to substorm injections.

In order to fully and correctly incorporate EMIC waves into global radiation belt and ring current models, we must understand the conditions under which the waves are observed, which we address in this paper, and when and how the waves interact with different particle populations. We leave the latter for future work.

Acknowledgments

The Van Allen Probes EMFISIS data are available at <http://emfisis.physics.uiowa.edu/>, EFW data at <http://www.space.umn.edu/rbspew-data/>, and HOPE and MagEIS data at <https://rbsp-ect.lanl.gov/>. The authors thank Craig Kletzing for the EMFISIS data. The GOES satellite data are available at the website: <https://satdat.ngdc.noaa.gov/sem/goes/data/>. The solar wind parameters and geomagnetic indices are available at OMNI/CDWeb: <https://omniweb.gsfc.nasa.gov/>. The LANL satellite energetic particle data are provided by Geoff Reeves. The authors thank I. R. Mann, D. K. Milling, and the rest of the CARISMA team for the data. CARISMA is operated by the University of Alberta, funded by the Canadian Space Agency. Ground station SNKQ is part of the NRCan (Natural Resources Canada) network operated by Geological Survey of Canada. Portions of this research were funded by the Van Allen Probes mission. Work at the University of Minnesota was supported by JHU/APL contract UMN 922613 under NASA contract JHU/APL NASS-01072.

References

- Akasofu, S. (1968). *Polar and magnetospheric substorms*. Springer-Verlag New York: Astrophysics and space science library.
- Allen, R. C., Zhang, J.-C., Kistler, L. M., Spence, H. E., Lin, R.-L., Klecker, B., et al. (2016). A statistical study of EMIC waves observed by Cluster 2. Associated plasma conditions. *Journal of Geophysical Research: Space Physics*, 121, 6458–6479. <https://doi.org/10.1002/2016JA022541>
- Anderson, B. J., Erlanson, R. E., & Zanetti, L. J. (1992). A statistical study of Pc 1-2 magnetic pulsations in the equatorial magnetosphere: 1. Equatorial occurrence distributions. *Journal of Geophysical Research*, 97, 3075–3088. <https://doi.org/10.1029/91JA02706>
- Anderson, B. J., & Hamilton, D. C. (1993). Electromagnetic ion cyclotron waves stimulated by modest magnetospheric compressions. *Journal of Geophysical Research*, 98, 11,369–11,382. <https://doi.org/10.1029/93JA00605>
- Angelopoulos, V. (2008). The THEMIS mission. *Space Science Reviews*, 141, 5–34. <https://doi.org/10.1007/s11214-008-9336-1>
- Blake, J. B., Carranza, P. A., Claudepierre, S. G., Clemmons, J. H., Crain, W. R., Dotan, J., et al. (2013). The Magnetic Electron Ion Spectrometer (MagEIS) instruments aboard the Radiation Belt Storm Probes (RBSP) spacecraft. *Space Science Reviews*, 179, 1–4. <https://doi.org/10.1007/S11214-013-9991-8>
- Blum, L. W., Halford, A. J., Millan, R., Bonnelli, J. W., Goldstein, J., Usanova, M., et al. (2015). Observations of coincident EMIC wave activity and duskside energetic electron precipitation on 18–19 January 2013. *Geophysical Research Letters*, 42, 5727–5735. <https://doi.org/10.1002/2015GL065245>
- Bortnik, J., Cutler, J. W., Dunson, C., Bleier, T. E., & McPherron, R. L. (2008). Characteristics of low latitude Pc1 pulsations during geomagnetic storms. *Journal of Geophysical Research*, 113, A04201. <https://doi.org/10.1029/2007JA012867>
- Bräysy, T., Mursula, K., & Marklund, G. (1998). Ion cyclotron waves during a great magnetic storm observed by Freja double-probe electric field instrument. *Journal of Geophysical Research*, 103(A3), 4145–4155. <https://doi.org/10.1029/97JA02820>
- Cho, J.-H., Lee, D.-Y., Noh, S.-J., Shin, D.-K., Hwang, J., Kim, K.-C., et al. (2016). Van Allen Probes observations of electromagnetic ion cyclotron waves triggered by enhanced solar wind dynamic pressure. *Journal of Geophysical Research: Space Physics*, 121, 9771–9793. <https://doi.org/10.1002/2016JA022841>
- Clilverd, M. A., Duthie, R., Hardman, R., Hendry, A. T., Rodger, C. J., Raita, T., et al. (2015). Electron precipitation from EMIC waves: A case study from 31 May 2013. *Journal of Geophysical Research: Space Physics*, 120, 3618–3631. <https://doi.org/10.1002/2015JA021090>
- Cornwall, J. M. (1965). Cyclotron instabilities and electromagnetic emission in the ultra low frequency and very low frequency ranges. *Journal of Geophysical Research*, 70(1), 61–69. <https://doi.org/10.1029/JZ070i001p00061>

- Cornwall, J. M., Coroniti, F. V., & Thorne, R. M. (1970). Turbulent loss of ring current protons. *Journal of Geophysical Research*, *75*(25), 4699–4709. <https://doi.org/10.1029/JA075i025p04699>
- Cornwall, J. M., & Schulz, M. (1971). Electromagnetic ion-cyclotron instabilities in multicomponent magnetospheric plasmas. *Journal of Geophysical Research*, *76*, 7791–7796. <https://doi.org/10.1029/JA076i031p07791>
- Criswell, D. R. (1969). Pc 1 micropulsation activity and magnetospheric amplification of 0.2 to 5.0 Hz hydromagnetic waves. *Journal of Geophysical Research*, *74*, 205–224. <https://doi.org/10.1029/JA074i001p0205>
- Elkington, S. R., Bakerm, D. N., & Wiltberger, M. (2005). Injection of energetic ions during the 31 March 0630 substorm. <https://doi.org/10.1029/155GM17>
- Engebretson, M. J., Lessard, M. R., Bortnik, J., Green, J. C., Horne, R. B., Detrick, D. L., et al. (2008). Pc1-Pc2 waves and energetic particle precipitation during and after magnetic storms: Superposed epoch analysis and case studies. *Journal of Geophysical Research*, *113*, A01211. <https://doi.org/10.1029/2007JA012362>
- Engebretson, M. J., Peterson, W. K., Posch, J. L., Klatt, M. R., Anderson, B. J., Russell, C. T., et al. (2002). Observations of two types of Pc 1–2 pulsations in the outer dayside magnetosphere. *Journal of Geophysical Research*, *107*(A12), 1451. <https://doi.org/10.1029/2001JA000198>
- Engebretson, M. J., Posch, J. L., Wygant, J. R., Kletzing, C. A., Lessard, M. R., Huang, C.-L., et al. (2015). Van Allen probes, NOAA, GOES, and ground observations of an intense EMIC wave event extending over 12 h in magnetic local time. *Journal of Geophysical Research: Space Physics*, *120*, 5465–5488. <https://doi.org/10.1002/2015JA021227>
- Erlanson, R. E., & Ukhorskiy, A. J. (2001). Observations of electromagnetic ion cyclotron waves during geomagnetic storms: Wave occurrence and pitch angle scattering. *Journal of Geophysical Research*, *106*(A3), 3883–3895. <https://doi.org/10.1029/2000JA000083>
- Erlanson, R. E., Zanetti, L. J., Potemra, T. A., Block, L. P., & Holmgren, G. (1990). Viking magnetic and electric field observations of Pc 1 waves at high latitudes. *Journal of Geophysical Research*, *95*, 5941–5955.
- Fraser, B. J., Singer, H. J., Adrian, M., & Gallagher, D. L. (2005). *The relationship between plasma density structure and EMIC waves at geosynchronous orbit*. *Geophys. Monogr. Ser.* (Vol. 159, pp. 55–70). Washington DC: AGU.
- Frey, H. U., & Mende, S. B. (2006). Substorm onsets as observed by IMAGE-FUV. *International Conference on Substorms*, *8*, 71–75.
- Frey, H. U., Mende, S. B., Angelopoulos, V., & Donovan, E. F. (2004). Substorm onset observations by IMAGE-FUV. *Journal of Geophysical Research*, *109*, A10304. <https://doi.org/10.1029/2004JA010607>
- Fukunishi, H. (1973). Occurrence of IPDP events accompanied by cosmic noise absorption in the course of proton aurora substorms. *Journal of Geophysical Research*, *78*(19), 3981–3986. <https://doi.org/10.1029/JA078i019p03981>
- Funsten, H. O., Skoug, R. M., Guthrie, A. A., MacDonald, E. A., Baldonado, J. R., Harper, R. W., et al. (2013). Helium, Oxygen, Proton, and Electron (HOPE) mass spectrometer for the Radiation Belt Storm Probes mission. *Space Science Reviews*, *179*, 1–4. <https://doi.org/10.1007/s11214-013-9968-7>
- Gendrin, R. (1970). Substorm aspects of magnetic pulsations. *Space Science Reviews*, *11*(1), 54–130. <https://doi.org/10.1007/BF00174429>
- Halford, A. J., Fraser, B. J., & Morley, S. K. (2010). EMIC wave activity during geomagnetic storm and nonstorm periods: CRRES results. *Journal of Geophysical Research*, *115*, A12248. <https://doi.org/10.1029/2010JA015716>
- Halford, A. J., Fraser, B. J., Morley, S. K., Elkington, S. R., & Chan, A. A. (2016). Dependence of EMIC wave parameters during quiet, geomagnetic storm, and geomagnetic storm phase times. *Journal of Geophysical Research: Space Physics*, *121*, 6277–6291. <https://doi.org/10.1002/2016JA022694>
- Hayakawa, M., Shimakura, S., Kobayashi, T., & Sato, N. (1992). A study of polarization of irregular pulsations of diminishing period and their generation mechanism. *Planetary and Space Science*, *40*(8), 1081–1091. [https://doi.org/10.1016/0032-0633\(92\)90037-O](https://doi.org/10.1016/0032-0633(92)90037-O)
- He, Z., Chen, L., Zhu, H., Xia, Z., Reeves, G. D., Xiong, Y., et al. (2017). Multiple-satellite observation of magnetic dip event during the substorm on 10 October 2013. *Geophysical Research Letters*, *44*, 9167–9175. <https://doi.org/10.1002/2017GL074869>
- Heacock, R. R. (1967). Evening micropulsation events with a rising midfrequency characteristic. *Journal of Geophysical Research*, *72*(1), 399–408. <https://doi.org/10.1029/JZ072i001p00399>
- Heacock, R. R., & Akasofu, S.-I. (1973). Periodically structured pc 1 micropulsations during the recovery phase of intense magnetic storms. *Journal of Geophysical Research*, *78*(25), 5524–5536. <https://doi.org/10.1029/JA078i025p05524>
- Ishida, J., Kokubun, S., & McPherron, R. L. (1987). Substorm effects on spectral structures of Pc 1 waves at synchronous orbit. *Journal of Geophysical Research*, *92*(A1), 143–158. <https://doi.org/10.1029/JA092iA01p00143>
- Jacobs, J. A. (1970). (1st ed.), *Geomagnetic micropulsations, physics and chemistry in space* (Vol. 1, pp. 179). Berlin, Heidelberg: Springer-Verlag Berlin Heidelberg. <https://doi.org/10.1007/978-3-642-86828-3>
- Jordanova, V. K., Albert, J., & Miyoshi, Y. (2008). Relativistic electron precipitation by EMIC waves from self-consistent global simulations. *Journal of Geophysical Research*, *113*, A00A10. <https://doi.org/10.1029/2008JA013239>
- Jordanova, V., Farrugia, C., Thorne, R., Khazanov, G. V., Reeves, G., & Thomsen, M. (2001). Modeling ring current proton precipitation by EMIC waves during the May 14–16, 1997, storm. *Journal of Geophysical Research*, *106*(A1), 7–22. <https://doi.org/10.1029/2000JA002008>
- Kangas, J., Aikio, A., & Olson, J. V. (1986). Multistation correlation spectra associated with sudden impulses. *Planetary and Space Science*, *34*, 543. [https://doi.org/10.1016/0032-0633\(86\)90092-9](https://doi.org/10.1016/0032-0633(86)90092-9)
- Kasahara, Y., Sawada, A., Yamamoto, M., Kimura, I., Kokubun, S., & Hayashi, K. (1992). Ion cyclotron emissions observed by the satellite Akebono in the vicinity of the magnetic equator. *Radio Science*, *27*(2), 347–362. <https://doi.org/10.1029/91RS01872>
- Keika, K., Nose, M., Brandt, P., Ohtani, S., Mitchell, D. G., & Roelof, E. C. (2006). Contribution of charge exchange loss to the storm time ring current decay: IMAGE/HENA observations. *Journal of Geophysical Research*, *111*, A11S12. <https://doi.org/10.1029/2006JA011789>
- Keika, K., Takahashi, K., Ukhorskiy, A. Y., & Miyoshi, Y. (2013). Global characteristics of electromagnetic ion cyclotron waves: Occurrence rate and its storm dependence. *Journal of Geophysical Research: Space Physics*, *118*, 4135–4150. <https://doi.org/10.1002/jgra.50385>
- Kennel, C. F., & Petschek, H. E. (1966). Limit on stably trapped particle fluxes. *Journal of Geophysical Research*, *71*, 1–28. <https://doi.org/10.1029/JZ071i001p00001>
- Khazanov, G. V., Gamayunov, K. V., Gallagher, D. L., & Kozyra, J. U. (2006). Self-consistent model of magnetospheric ring current and propagating electromagnetic ion cyclotron waves: Waves in multi ion magnetosphere. *Journal of Geophysical Research*, *111*, A10202. <https://doi.org/10.1029/2006JA011833>
- Kim, G.-J., Kim, K.-H., Lee, D.-H., Kwon, H.-J., & Park, J.-S. (2016). Occurrence of EMIC waves and plasmaspheric plasmas derived from THEMIS observations in the outer magnetosphere: Revisit. *Journal of Geophysical Research: Space Physics*, *121*, 9443–9458. <https://doi.org/10.1002/2016JA023108>
- Kim, K.-H., Omura, Y., Jin, H., & Hwang, J. (2017). A case study of EMIC waves associated with sudden geosynchronous magnetic field changes. *Journal of Geophysical Research: Space Physics*, *122*, 3322–3341. <https://doi.org/10.1002/2016JA023391>
- Kletzing, C. A., Kurth, W. S., Acuna, M., MacDowall, R. J., Torbert, R. B., Averkamp, T., et al. (2013). The Electric and Magnetic Field Instrument Suite and Integrated Science (EMFISIS) on RBSP. *Space Science Reviews*, *179*, 127–181. <https://doi.org/10.1007/s11214-013-9993-6>

- Kozyra, J. U., Cravens, T. E., Nagy, A. F., Fontheim, E. G., & Ong, R. S. B. (1984). Effects of energetic heavy ions on electromagnetic ion cyclotron wave generation in the plasmopause region. *Journal of Geophysical Research*, *89*(A4), 2217–2233. <https://doi.org/10.1029/JA089IA04p02217>
- Kubota, Y., Omura, Y., & Summers, D. (2015). Relativistic electron precipitation induced by EMIC-triggered emissions in a dipole magnetosphere. *Journal of Geophysical Research: Space Physics*, *120*, 4384–4399. <https://doi.org/10.1002/2015JA021017>
- Li, W., Shprits, Y. Y., & Thorne, R. M. (2007). Dynamic evolution of energetic outer zone electrons due to wave-particle interactions during storms. *Journal of Geophysical Research*, *112*, A10220. <https://doi.org/10.1029/2007JA012368>
- Mann, I. R., Milling, D. K., Rae, I. J., Ozeke, L. G., Kale, A., Kale, Z. C., et al. (2008). The upgraded CARISMA magnetometer array in the THEMIS era. *Space Science Reviews*, *141*, 413–451. <https://doi.org/10.1007/s11214-008-9457-6>
- McPherron, R. L. (1970). Growth phase of magnetospheric substorms. *Journal of Geophysical Research*, *75*, 5592–5599. <https://doi.org/10.1029/JA075i028p05592>
- Mende, S. B., Harris, S. E., Frey, H. U., Angelopoulos, V., Russell, C. T., Donovan, E., et al. (2008). The THEMIS array of ground-based observatories for the study of auroral substorms. *Space Science Reviews*, *141*(1), 357–387. <https://doi.org/10.1007/978-0-387-89820-9-16>
- Meredith, N. P., Horne, R. B., Kersten, T., Fraser, B. J., & Grew, R. S. (2014). Global morphology and spectral properties of EMIC waves derived from CRRES observations. *Journal of Geophysical Research*, *119*, 5328–5342. <https://doi.org/10.1002/2014JA020064>
- Meredith, N. P., Thorne, R. M., Horne, R. B., Summers, D., Fraser, B. J., & Anderson, R. R. (2003). Statistical analysis of relativistic electron energies for cyclotron resonance with EMIC waves observed on CRRES. *Journal of Geophysical Research*, *108*(A6), 1250. <https://doi.org/10.1029/2002JA009700>
- Min, K., Lee, J., Keika, K., & Li, W. (2012). Global distribution of EMIC waves derived from THEMIS observations. *Journal of Geophysical Research*, *117*, A05219. <https://doi.org/10.1029/2012JA017515>
- Miyoshi, Y., Sakaguchi, K., Shiokawa, K., Evans, D., Albert, J., Connors, M., & Jordanova, V. (2008). Precipitation of radiation belt electrons by EMIC waves, observed from ground and space. *Geophysical Research Letters*, *35*, L23101. <https://doi.org/10.1029/2008GL035727>
- Olson, J. V., & Lee, L. C. (1983). Pc1 wave generation by sudden impulses. *Planetary and Space Science*, *31*(3), 295–297. [https://doi.org/10.1016/0032-0633\(83\)90079-X](https://doi.org/10.1016/0032-0633(83)90079-X)
- Park, J.-S., Kim, K.-H., Shiokawa, K., Lee, D.-H., Lee, E., Kwon, H.-J., et al. (2016). EMIC waves observed at geosynchronous orbit under quiet geomagnetic conditions ($Kp \leq 1$). *Journal of Geophysical Research: Space Physics*, *121*, 1377–1390. <https://doi.org/10.1002/2015JA021968>
- Posch, J. L., Engebretson, M. J., Murphy, M. T., Denton, M. H., Lessard, M. R., & Horne, R. B. (2010). Probing the relationship between electromagnetic ion cyclotron waves and plasmaspheric plumes near geosynchronous orbit. *Journal of Geophysical Research*, *115*, A11205. <https://doi.org/10.1029/2010JA015446>
- Reeves, G., Belian, R., Cayton, T., Christensen, R., Henderson, M., & McLachlan, P. (1996). Los Alamos space weather data products: On line and on time, in. In E. Rolfe, & B. Kaldeich (Eds.), *International conference on substorms, ESA special publication* (Vol. 389, pp. 689). Paris: European Space Agency.
- Reeves, G. D., Belian, R. D., & Fritz, T. A. (1991). Numerical tracing of energetic particle drifts in a model magnetosphere. *Journal of Geophysical Research*, *96*(A8), 13,997–14,008. <https://doi.org/10.1029/91JA01161>
- Remya, B., Tsurutani, B. T., Reddy, R. V., Lakhina, G. S., & Hajra, R. (2015). Electromagnetic cyclotron waves in the dayside subsolar outer magnetosphere generated by enhanced solar wind pressure: EMIC wave coherency. *Journal of Geophysical Research: Space Physics*, *120*, 7536–7551. <https://doi.org/10.1002/2015JA021327>
- Saikin, A. A., Zhang, J.-C., Smith, C. W., Spence, H. E., Torbert, R. B., & Kletzing, C. A. (2016). The dependence on geomagnetic conditions and solar wind dynamic pressure of the spatial distributions of EMIC waves observed by the Van Allen Probes. *Journal of Geophysical Research: Space Physics*, *121*, 4362–4377. <https://doi.org/10.1002/2016JA022523>
- Shoji, M., & Omura, Y. (2014). Spectrum characteristics of electromagnetic ion cyclotron triggered emissions and associated energetic proton dynamics. *Journal of Geophysical Research: Space Physics*, *119*, 3480–3489. <https://doi.org/10.1002/2013JA019695>
- Singer, H. J., Matheson, L., Grubb, R., Newman, A., & Bouwer, D. (1996). Monitoring space weather with the GOES magnetometers. In E. Washwell (Ed.), *GOES-8 and beyond* (Vol. 2812, pp. 299–308). Boulder, CO: NOAA Space Environment Center. <https://doi.org/10.1117/12.254077>
- Søråas, F., Lundblad, J. A., Maltseva, N. F., Troitskaya, V., & Selivanov, V. (1980). A comparison between simultaneous I.P.D.P. ground based observations and observations of energetic protons obtained by satellites. *Planetary and Space Science*, *28*(4), 387–405. [https://doi.org/10.1016/0032-0633\(80\)90043-4](https://doi.org/10.1016/0032-0633(80)90043-4)
- Southwood, D. J., & Kivelson, M. G. (1975). An approximate analytic description of plasma bulk parameters and pitch angle anisotropy under adiabatic flow in a dipolar magnetospheric field. *Journal of Geophysical Research*, *80*, 2069–2073. <https://doi.org/10.1029/JA080i016p02069>
- Spence, H., Reeves, G., Baker, D., Blake, J., Bolton, M., Bourdarie, S., et al. (2013). Science goals and overview of the Radiation Belt Storm Probes (RBSP) Energetic particle, Composition, and Thermal plasma (ECT) suite on NASA's Van Allen Probes mission. *Space Science Reviews*, *179*, 311–336. <https://doi.org/10.1007/s11214-013-0007-5>
- Summers, D., Thorne, R. M., & Xiao, F. (1998). Relativistic theory of wave-particle resonant diffusion with application to electron acceleration in the magnetosphere. *Journal of Geophysical Research*, *103*(A9), 20,487–20,500. <https://doi.org/10.1029/98JA01740>
- Tetrick, S. S., Engebretson, M. J., Posch, J. L., Olson, C. N., Smith, C. W., Denton, R. E., et al. (2017). Location of intense electromagnetic ion cyclotron (EMIC) wave events relative to the plasmopause: Van Allen Probes observations. *Journal of Geophysical Research: Space Physics*, *122*, 4064–4088. <https://doi.org/10.1002/2016JA023392>
- Thorne, R. M., & Horne, R. (1992). The contribution of ion-cyclotron waves to electron heating and SAR-arc excitation near the stormtime plasmopause. *Geophysical Research Letters*, *19*, 417–420. <https://doi.org/10.1029/92GL00089>
- Thorne, R. M., & Kennel, C. F. (1971). Relativistic electron precipitation during magnetic storm main phase. *Journal of Geophysical Research*, *76*(19), 4446–4453. <https://doi.org/10.1029/JA076i019p04446>
- Thorne, R. M., Smith, E. J., Fiske, K. J., & Church, S. R. (1974). Intensity variation of ELF hiss and chorus during isolated substorms. *Geophysical Research Letters*, *1*, 193–196. <https://doi.org/10.1029/GL001i005p00193>
- Troitskaya, V. A. (1967). Micropulsations and the state of the magnetosphere.
- Tsurutani, B. T., Hajra, R., Tanimori, T., Takada, A., Remya, B., Mannucci, A. J., et al. (2016). Heliospheric plasma sheet (HPS) impingement onto the magnetosphere as a cause of relativistic electron dropouts (REDs) via coherent EMIC wave scattering with possible consequences for climate change mechanisms. *Journal of Geophysical Research: Space Physics*, *121*, 10,130–10,156. <https://doi.org/10.1002/2016JA022499>
- Tsurutani, B. T., & Lakhina, G. S. (1997). Some basic concepts of wave-particle interactions in collisionless plasmas. *Reviews of Geophysics*, *35*(4), 491–501. <https://doi.org/10.1029/97RG02200>

- Tsurutani, B. T., Zhou, X.-Y., Vasyliunas, V. M., Haerendel, G., Arballo, J. K., & Lakhina, G. S. (2001). Interplanetary shocks, magnetopause boundary layers and dayside auroras: The importance of a very small magnetospheric region. *Surveys in Geophysics*, 22(2), 101–130. <https://doi.org/10.1023/A:1012952414384>
- Tsyganenko, N. A., & Sitnov, M. I. (2005). Modeling the dynamics of the inner magnetosphere during strong geomagnetic storms. *Journal of Geophysical Research*, 110, A03208. <https://doi.org/10.1029/2004JA010798>
- Turner, D. L., Fennell, J. F., Blake, J. B., Claudepierre, S. G., Clemmons, J. H., Jaynes, A. N., et al. (2017). Multipoint observations of energetic particle injections and substorm activity during a conjunction between Magnetospheric Multiscale (MMS) and Van Allen Probes. <https://doi.org/10.1002/2017JA024554>
- Usanova, M. E., Mann, I. R., Bortnik, J., Shao, L., & Angelopoulos, V. (2012). THEMIS observations of electromagnetic ion cyclotron wave occurrence—Dependence on AE, SYMH, and solar wind dynamic pressure. *Journal of Geophysical Research*, 117, A10218. <https://doi.org/10.1029/2012JA018049>
- Vasyliunas, V. M. (1976). An overview of magnetospheric dynamics. In B. M. McCormac (Eds.), *Magnetospheric Particles and Fields* (Vol. 58, pp. 99). Dordrecht, Netherlands: Springer.
- Wang, D., Yuan, Z., Yu, X., Huang, S., Deng, X., Zhou, M., & Li, H. (2016). Geomagnetic storms and EMIC waves: Van Allen Probe observations. *Journal of Geophysical Research: Space Physics*, 121, 6444–6457. <https://doi.org/10.1002/2015JA022318>
- Wentworth, R. C. (1964). Enhancement of hydromagnetic emissions after geomagnetic storms. *Journal of Geophysical Research*, 69, 2291–2298. <https://doi.org/10.1029/JZ069i011p02291>
- Wygant, J., Bonnell, J. W., Goetz, K., Bonnell, J. W., Goetz, K., Ergun, R. E., et al. (2013). The Electric Field and Waves Instruments on the Radiation Belt Storm Probes mission. *Space Science Reviews*, 179, 183–220. <https://doi.org/10.1007/s11214-013-0013-7>
- Yahnina, T. A., Yahnin, A. G., Kangas, J., Manninen, J., Evans, D. S., Demekhov, A. G., et al. (2003). Energetic particle counterparts for geomagnetic pulsations of Pc1 and IPDP types. *Annales de Geophysique*, 21, 2281–2292. <https://doi.org/10.5194/angeo-21-2281-2003>
- Yuan, Z., Xiong, Y., Huang, S., Deng, X., Pang, Y., Zhou, M., et al. (2014). Cold electron heating by EMIC waves in the plasmaspheric plume with observations of the Cluster satellite. *Geophysical Research Letters*, 41, 1830–1837. <https://doi.org/10.1002/2014GL059241>
- Zhang, J.-C., Kistler, L. M., Mouikis, C. G., Dunlop, M. W., Klecker, B., & Sauvaud, J.-A. (2010). A case study of EMIC wave-associated He^+ energization in the outer magnetosphere: Cluster and Double Star 1 observations. *Journal of Geophysical Research*, 115, A06212. <https://doi.org/10.1029/2009JA014784>
- Zhou, Q., Xiao, F., Yang, C., He, Y., & Tang, L. (2013). Observation and modeling of magnetospheric cold electron heating by electromagnetic ion cyclotron waves. *Journal of Geophysical Research: Space Physics*, 118, 6907–6914. <https://doi.org/10.1002/2013JA019263>